RSC Advances

PAPER

View Article Online
View Journal | View Issue

Cite this: *RSC Adv.*, 2025, **15**, 6564

Preparation and characterization of electrically conductive nano-ZnO-doped Ti/Zr composite conversion coating on aluminum alloy

Aihua Yi,[a] Yuying Liu,[b] Jian Huang,[a] Jianyong Liu,[a] Xiaolan Chen,[a] Min Wang*[c] and Jingfeng Xie[d]

The integration of semiconductive nano-ZnO into a Ti/Zr-based solution has facilitated the development of a conductive coating on aluminum alloy surfaces. A comprehensive characterization of the coating's morphology, microstructure, electrical conductivity, and corrosion resistance was conducted utilizing a suite of analytical techniques, including SEM, FIB-SEM, EDS, XPS, UV-vis, FTIR, and an electrochemical workstation. Significantly, the electrical contact resistance (ECR) of the coating experienced a substantial decrease when subjected to a pressure of 200 psi, plummeting from 0.1907 Ω in^{-2} in the absence of nano-ZnO to 0.0621 Ω in^{-2} with the inclusion of nano-ZnO. Concurrently, the band gap of the coating was observed to diminish from 3.189 eV without nano-ZnO to 2.708 eV with nano-ZnO, indicating improved semiconductor properties. The coating exhibited a three-layer structure consisting of a substrate-close layer of nano-ZnO, a middle layer composed of Na_3AlF_6 crystals, and an outermost layer comprising ZnO and metal–organic complexes. The incorporation of nano-ZnO induced a striking morphological transition from a pebble-like to a cubic structure, along with a notable change in the coating's color. These findings collectively demonstrate the transformative impact of nano-ZnO on the multifaceted attributes of the conversion coating, endowing it with superior electrical characteristics.

Received 3rd September 2024
Accepted 13th December 2024

DOI: 10.1039/d4ra06350c

rsc.li/rsc-advances

1 Introduction

Aluminum and its alloys are characterized by lightweight, high specific strength, good toughness, ease of forming, and excellent machinability, and are widely used in various fields such as electronics, aerospace, automotive, machinery manufacturing, and chemical engineering.[1–3] However, aluminum alloys have poor corrosion resistance and require strict surface corrosion treatment before use. Unlike other fields, when aluminum alloys are used in the field of electronics, it is required that the surface of the aluminum alloy has both conductivity and corrosion resistance.[4,5] The chemical conversion coating has the advantages of convenience, speed, low cost and outstanding protection, and is therefore widely used for the surface treatment of aluminum alloys.[6,7]

By far the most established method in the field of chemical conversion of aluminum alloys is the chromate conversion method, which not only has excellent corrosion resistance but also has good electrical conductivity at the same time. The chromate method had been banned because of the toxicity of "hexavalent chromium".[8] Therefore, in recent years, the research focus has shifted towards finding alternative technologies for chromate, with particular emphasis on the corrosion resistance and adhesion properties of coatings prepared using these alternatives. However, comparatively less attention and research have been dedicated to the conductivity of such coatings. The addition of nanoparticles to the treatment solution to modify the coating is a relatively common method,[8–11] for example, Bagheri-Mohagheghi[11] *et al.* reported iron (Fe) doped tin oxide coatings, the coating have shown p-type conductivity. Li[12] *et al.* reported that a coating with certain electrical conductivity was prepared by doping antimony-tin oxide (ATO) particles in a micro-arc oxide (MAO) coating of AZ31 magnesium alloy, and the ECR of the coating was only 4.5 Ω cm^2.

ZnO is an oxide semiconductor material with a wide band gap energy (3.3 eV) and is widely used in optical, electronic, sensing, catalytic and photocatalytic applications.[13–16] Ruolin Yan[17] *et al.* reported on the preparation methods of conductive nano-ZnO and its high-temperature stability. Jeong S. H.[18] *et al.* used radio frequency magnetron sputtering technology to prepare aluminum-doped ZnO (AZO) coatings, with a resistivity of approximately 0.00098 Ω cm. However, the incorporation of nano-ZnO with electrical conductivity into the chemical conversion process to enhance the coating's electrical conductivity has been scarcely documented in existing literature. Based

[a]*Guangzhou City Polytechnic, Guangzhou, 510405, China*
[b]*School of Materials Science and Engineering, Dongguan University of Technology, Dongguan, 523808, China*
[c]*College of Mechanical Engineering, Guangdong Polytechnic Normal University, Guangzhou, 510302, China. E-mail: winawang@163.com*
[d]*Guangdong City Test Technology Co., Ltd, Guangzhou, 510106, China*

on previous studies by the authors,[19,20] the Ti/Zr coating was obtained by adding nano-ZnO, and the ECR of the coating was significantly reduced, and the mechanism of the action of nano-ZnO was discussed.

2 Materials and methods

2.1 Coating preparation

The sample material is 6063 aluminum alloy, from Guangdong Huachang Aluminum Co., Ltd. The sample was polished in a step-by-step manner using sandpapers of 600#, 800#, 1000# and 1200# grit, and then underwent alkali washing to remove oil (10 g per L NaOH, 8 g per L Na_2CO_3, 12 g per L Na_3PO_4) and pickling activation (5% HNO_3), and then rinsed with distilled water for use.

H_2TiF_6, H_2ZrF_6, tannic acid and nano-ZnO were successively added into distilled water to prepare a mixed solution containing 3.5 g per L H_2TiF_6, 0.5 g per L H_2ZrF_6, 3.5 g per L tannic acid and 2.0 g per L nano-ZnO. Then add a small amount of NaOH solution to adjust the pH to about 4.5, and finally ultrasonic dispersion for 30 minutes. The pretreated aluminum alloy samples are immersed in the ultrasonic solution, and the maximum processing time is 7 min. The concentration of nano-ZnO was optimized based on our previous systematic experiments utilizing both orthogonal and single-factor approaches. Nano-ZnO is obtained from Beijing Dekedao Gold Technology Co., Ltd, with an average particle size of about 30 nm and a density of 5.61 g cm^{-3}.

2.2 Characterization

The surface morphology and chemical composition of the coating was examined using a Veriosg4UC-FEI field emission scanning electron microscopy (FESEM) coupled with electron dispersive spectroscopy (EDS), at an acceleration voltage of 20 kV. The cross-section morphology Focused Ion Beam Scanning Electron Microscopes (FIB-SEM) measurement was conducted in a Thermo Scientific Helios G4 PFIB to characterize the morphology of the coating cross-section. X-ray Photoelectron Spectroscopy (XPS) measurement was conducted in a Kratos Axis Ultra DLD equipped with a standard Al Ka X-ray source (1486.6 eV) and a hemispherical analyzer. The pressure in the specimen chamber was kept at about 1×10^{-9} mbar. The standard binding energy of C 1s peak (284.6 eV) was adopted to calibrate binding energies in the XPS spectra. The FTIR analysis was performed using a Bruker Vertex 70 type spectrometer in transmission mode at a resolution of 4 cm^{-1}, with four scans per sample. The infrared spectra were recorded in absorbance units in the 4000–400 cm^{-1} range.

ECR measurements were obtained based on the integrated test system designed according to the Mil-DTL-5541F standard. ECR values were collected using a Model 1750 Micro-Ohmmeter with an accuracy of 0.02% at room temperature. Resistance values were obtained by applying a constant load on the copper electrode applied by the servo compression tester (FR-108C) for 5 min at a load range of 50 psi (0.344 MPa) to 200 psi (1.38 MPa) with a fluctuation area of 1 in^2 (6.45 cm^2) above and below the electrode within 2% of the required pressure. Each sample was tested five times to obtain good reproducibility. The UV spectrum (Hitachi UH4150) was measured by diffuse reflectance method with a measuring range of 200–800 nm and a step size of 1 nm.

The corrosion resistance of the coating was evaluated by potentiodynamic polarization curve which was recorded with the Princeton Applied VersaSCAN workstation. The measurement was performed in electrolyte of NaCl (3.5 wt%). A conventional three-electrode cell was used for all the electrochemical tests, with a Ag/AgCl (0.6 mol per L KCl) reference electrode and a platinum counter electrode. The working electrode was the studied alloy with an area of 1.0 cm^2 exposed to the aggressive solution. The potential was scanned at a rate of 0.5 mV s^{-1} and scanning ranged from −1.3 V to −0.6 V.

3 Results and discussion

The image in Fig. 1(a) illustrates the coatings obtained without nano-ZnO, while Fig. 1(b) exhibits the coatings obtained with nano-ZnO. It is evident from Fig. 1 that the addition of nano-ZnO modifies the color of the coating from yellow to navy blue. Further examination of the microstructure of both types of coatings was conducted using SEM and is presented in Fig. 2. Previous studies[19] indicate that the particles depicted in Fig. 2(a) and (b) are Na_3AlF_6 crystals. Notably, as shown in Fig. 2(b), nano-ZnO has infiltrated into the coating and filled gaps between Na_3AlF_6 crystals. Both figures illustrate that incorporating nano-ZnO not only alters the color but also modifies the microscopic morphology, transitioning it from a pebble-like shape to a cubic. Table 1 presents EDS results for an area highlighted in Fig. 2(b), revealing a Zn element content of approximately 3.99% (at%).

SEM analysis was conducted on coatings with varying formation times (30 s, 120 s, 240 s, and 420 s) to investigate the infiltration of nano-ZnO into the coating. The results are illustrated in Fig. 3(a–d) and 2b, where Fig. 3(d) displays a magnified image of a coating formed for 420 seconds. The figures reveal that nano-ZnO fills the gaps between Na_3AlF_6 crystal particles. Table 2 presents the findings from EDS mapping study performed on the coating. It shows that nano-ZnO particles infiltrated the coating within the first thirty seconds of its

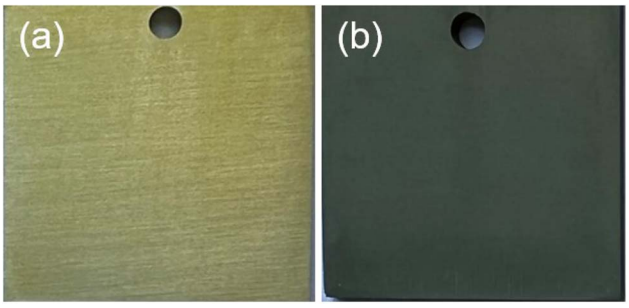

Fig. 1 Photos of specimen with conversion coating: without ZnO (a), with ZnO(b).

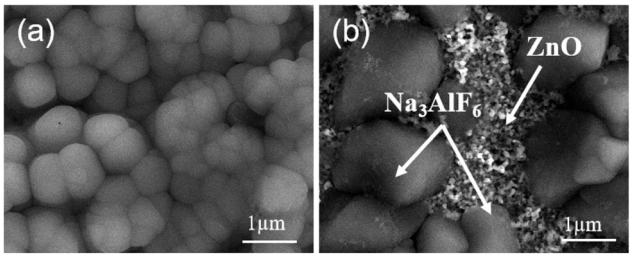

Fig. 2 SEM of specimen with conversion coating: without ZnO (a), with ZnO(b).

formation. As formation time increases and Na_3AlF_6 crystals continue to develop, there is an upward trend in nano-ZnO concentration within the coating. A small portion of nano-ZnO combines with tannic acid to form complexes on the surface while most of it is sandwiched between large Na_3AlF_6 particles creating conductive channels that enhance electrical conductivity.

The FIB-SEM cross-section of the coating is illustrated in Fig. 4. The figure reveals that Na_3AlF_6 particles are growing on the surface of the aluminum substrate. Nano-ZnO and titanium compounds predominantly cover the entire surface of Na_3AlF_6 particles, thereby creating favorable conditions for reducing ECR at the coating surface. Additionally, some nano-ZnO and titanium compounds are found within the interstitial spaces between Na_3AlF_6 particles and the substrate. This suggests that nano-ZnO primarily resides on the coating's surface, filling the voids between Na_3AlF_6 crystal particles and lying adjacent to the substrate.

Fig. 5 exhibits the FTIR spectrum obtained from coatings with and without nano-ZnO. Absorption peaks around wavenumbers of approximately 3421 cm^{-1} and 561 cm^{-1} are evident in both cases. The bands around 3421 cm^{-1} are attributed to the –OH, and 561 cm^{-1} is attributed to the Na_3AlF_6. In contrast, when no nano-ZnO is present in the coating formulation, the absorption peak associated with C=O stretching vibration appears at a wavenumber value close to 1691 cm^{-1}; however, when incorporating nano-ZnO into tannic acid hydrolysis product (trihydroxybenzoic acid), this absorption peak shifts towards a lower number value (~1658 cm^{-1}),[19,20] indicating occurrence of some reaction between nano-ZnO and trihydroxybenzoic acid.

The FTIR spectrum of the coating shows several characteristic peaks of benzene rings at 1550–1000 cm^{-1}. Compared with the FTIR spectrum of the coating obtained without nano-ZnO, the peaks located in the region are appreciably changed, which signifies that the substituent groups on the benzene ring are changed.[21,22] There are two main reasons for the change in the peaks of the benzene ring.[19] First, there is a change in the quantity of substituents attached to the benzene ring; second,

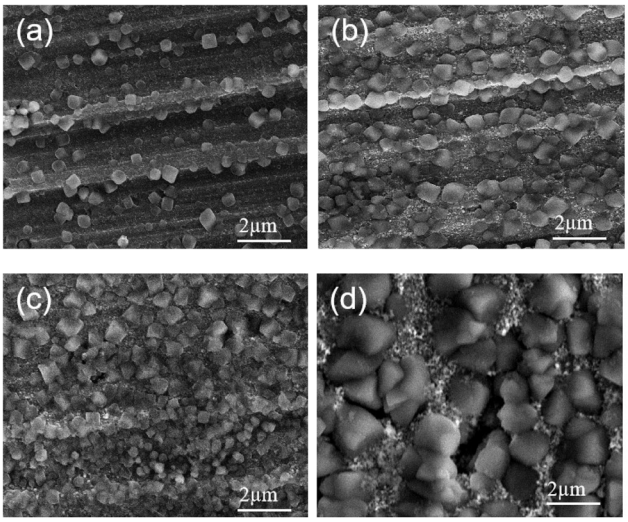

Fig. 3 SEM images the surface of the samples treated in the conversion solution for different time: 30 s (a), 120 s (b), 240 s (c), 420 s (d).

Table 2 Nano-ZnO content (at%) in coating with different formation times

Time/s	30	120	240	420
ZnO(atomic)/%	0.93	5.94	4.56	3.99

the number of substituents in the benzene ring does not change, but the substituents react with other substances, resulting in a change in the chemical environment surrounding of the benzene ring. In this study, the change of the peaks of the benzene ring are mainly due to the combination of the vacant orbital on Zn atom in nano-ZnO with the O atom on trihydroxybenzoic acid, which changes the chemical environment of the benzene ring. In this study, the change of the characteristic absorption peak of the benzene ring is mainly due to the abundant electron combination between the vacant orbital of Zn atom in nano-ZnO and the O atom of trihydroxybenzoic acid, which changes the chemical environment of the benzene ring.

Fig. 6 show the details of peaks of Zn 2p element. The Zn 2p core-level spectrum could be curved-fitted into two peak components. The peak located at 1022.0 eV and 1023.4 eV can be assigned to ZnO and Zn complex, respectively.[23–28] The results show that ZnO reacts with trihydroxybenzoic acid, the hydrolyzed product of tannic acid, which is consistent with the infrared analysis results.

Fig. 7 shows the ECR of the coatings obtained with and without nano-ZnO under different pressures. The ECR values decrease with the increase of pressure load. The load can change the contact characteristics between the material surface and the test electrode. When the pressure increases, the

Table 1 The element of the conversion coating (with ZnO)

Element	C	O	F	Na	Mg	Al	Ti	Zn	Zr	Total
Atomic/%	15.06	9.99	37.32	16.90	0.52	14.93	1.12	3.99	0.16	100

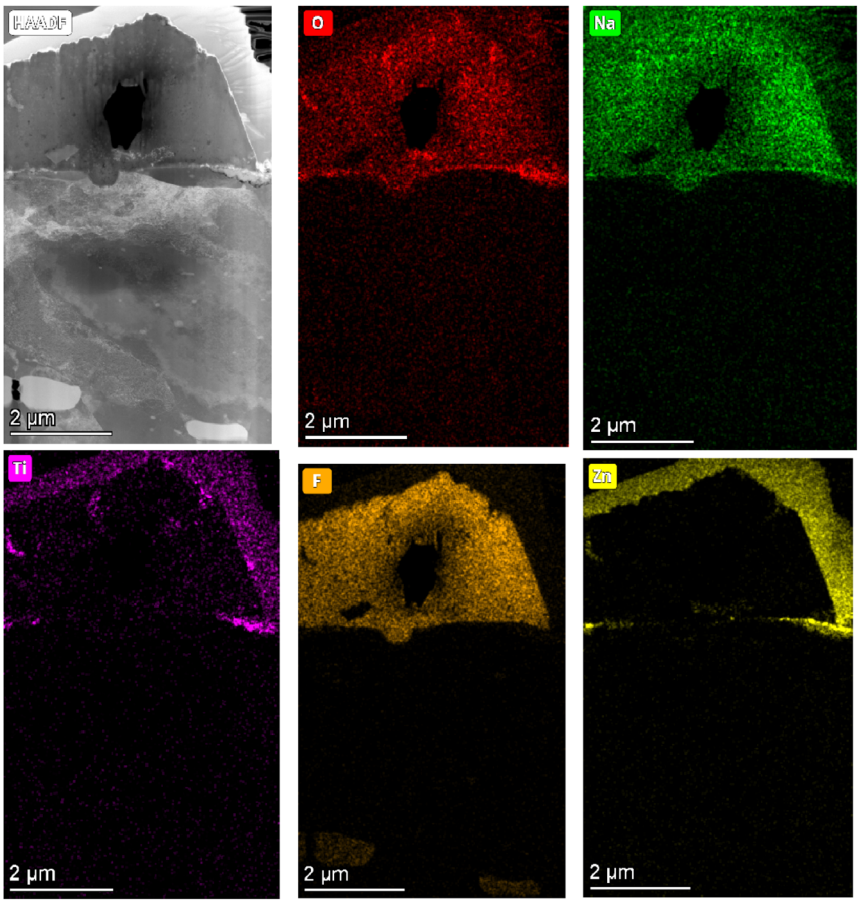

Fig. 4 Cross-sectional images (FIB-SEM) of the coating.

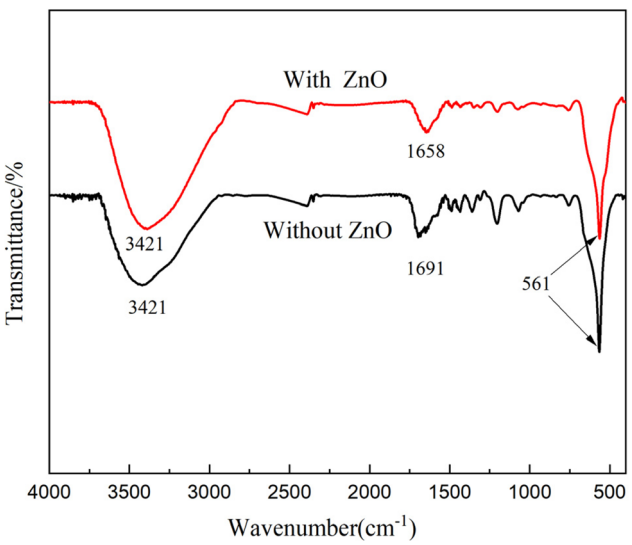

Fig. 5 FTIR spectrum of the coating obtained with and without nano-ZnO.

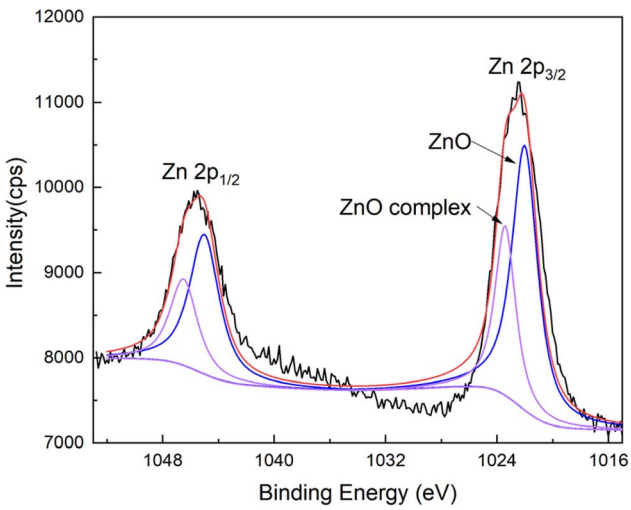

Fig. 6 XPS spectra of Zn 2p of the conversion coating.

deformation of the coating increases, the actual contact area increases, and the number of contact points increases, thus the power supply current conduction in more conductive areas increases, and the ECR decreases. With the addition of nano-ZnO, a connected grid is formed on the surface of the coatings, which substantially diminishes the electrical contact resistance (ECR) and markedly enhances electrical conductivity. Specifically, the ECR values exhibit a notable reduction,

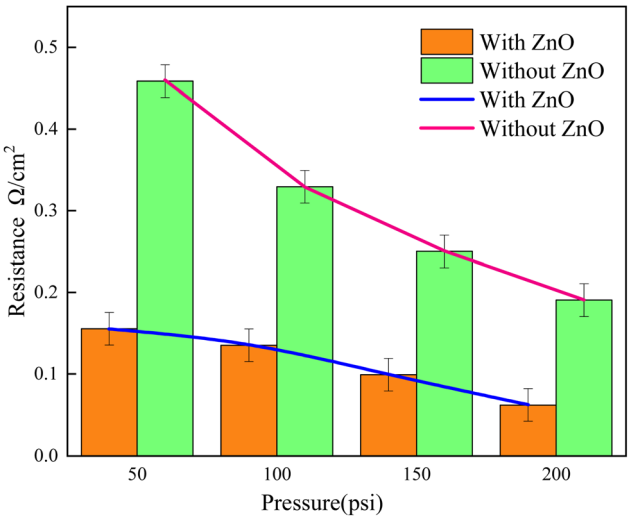

Fig. 7 ECR of the coatings obtained with and without nano-ZnO under different pressures.

dropping from 0.197 Ω in^{-2} (without nano-ZnO) to 0.0621 Ω in^{-2} (with nano-ZnO), as measured under a pressure of 200 psi.

Fig. 8 shows the polarization curves of the coatings with/without nano-ZnO. The corrosion current density (i_{corr}) and self-corrosion potential (E_{corr}) are important parameters to characterize the corrosion resistance of the coating. The current density corresponding to the intersection of the tangent line of the anode region and the tangent line of the cathode region is the corrosion current density (i_{corr}). The intersection of the anode curve and the cathode curve is the self-corrosion potential (E_{corr}). The corrosion current density (i_{corr}) of the coatings obtained with and without nano-ZnO were 5.19 μA cm^{-2} and 6.42 μA cm^{-2}, respectively. The values of self-corrosion potential (E_{corr}) for coatings without nano-ZnO is −992 mV, while that for with nano-ZnO is −778 mV. The E_{corr} with nano-ZnO samples shifts about 214 mV towards the positive direction compared to the without nano-ZnO. Obviously, base on the i_{corr} and E_{corr}, the corrosion resistance of the coatings with nano-ZnO could be slightly improved by adding nano-ZnO.

EIS can give important information on corrosion activity during immersion in the corrosive media. In Nyquist plots, the diameter of the arc is an important parameter, the bigger the diameter of the arc, the better the corrosion resistance. As for Nyquist plot curves illustrated in Fig. 9, the arc diameter of the coating with and without nano-ZnO is roughly the same, indicating that the addition of nano-ZnO has little effect on the corrosion resistance of the coating. On the other hand, at high frequency, two coatings with and without nano-ZnO have the obvious capacitive loop, it means that the coating on the substrate makes the electrochemical reaction weaken. These results indicate that the addition of nano-ZnO has a slight effect on the corrosion resistance of the coating.

The band gap width is one of the important parameters to measure the conductivity of semiconductor materials.[29] The smaller the band gap, the better the conductivity. The diffuse UV visible absorption spectrum of the two coatings were analyzed, and the bandgap energy was calculated according to Kubelka–Munk theory. The band gap width (E_g) of semiconductors is closely related to absorption coefficient (A) and photon energy ($h\nu$), which can be described by Tauc equation:[30,31]

$$A\hbar\nu = k(\hbar\nu - E_g)^{1/2}$$

where, A is the absorption coefficient, h is the Planck constant, ν is the optical frequency, k is a constant, generally set as 1. Using $h\nu = 1240/\lambda$ as the horizontal coordinate (λ is the wavelength) and $(Ah\nu)^2$ as the vertical coordinate for the graph, a tangent line is made to the curve in the graph and the intercept of the tangent line is the band gap width E_g. UV-vis absorption spectrum of the coatings is shown in Fig. 10. It can be seen from the figure that, the band gap of the coating obtained without nano-

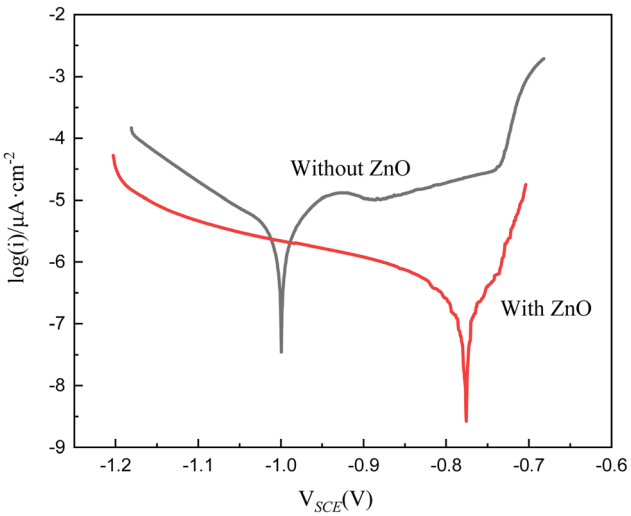

Fig. 8 Tafel curves of the coating obtained with and without nano-ZnO.

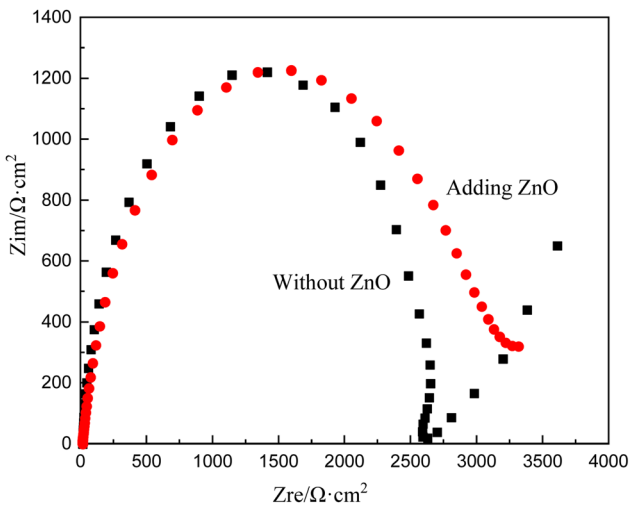

Fig. 9 EIS Nyquist plots of coating obtained with and without nano-ZnO.

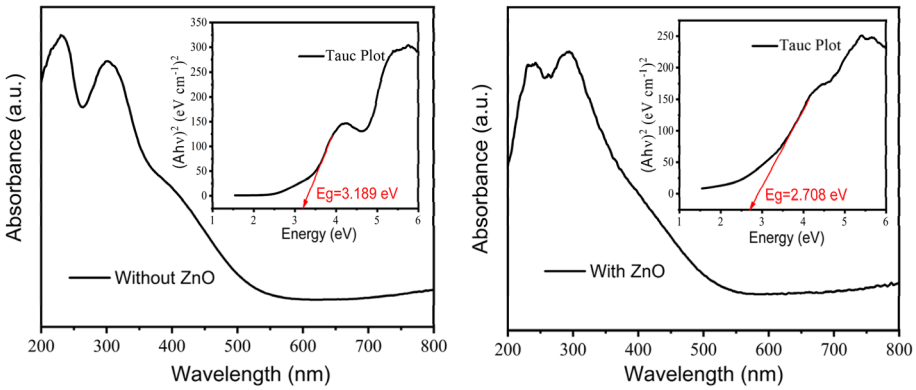

Fig. 10 UV-vis absorption spectrum of the coatings.

ZnO is 3.189 eV, while the band gap with nano-ZnO is 2.708 eV. The addition of nano-ZnO improves the conductivity of the coating, which is consistent with the ECR results. The UV cutoff wavelength of the coating without nano-ZnO (about 290 nm) is larger than that with nano-ZnO (about 230 nm). The larger the UV cutoff wavelength, the smaller the band gap and the better the conductivity,[32] which is consistent with the result of the band gap. Through the analysis of corrosion resistance and electrical conductivity, it can be seen that the addition of nano-ZnO has little effect on the corrosion resistance of the coating, but it can significantly improve the electrical conductivity of the coating. The ECR is reduced from 0.197 Ω in^{-2} (without nano-ZnO) to 0.0621 Ω in^{-2} (with nano-ZnO) at 200 psi, and the band gap is reduced from 3.189 eV (without nano-ZnO) to 2.708 eV (with nano-ZnO).

4 Discussion

ZnO has emerged as an important material in conductive oxides that can be used in low-resistive and highly-transparent electrodes composed of abundantly available and environmentally-friendly elements. Shirahata *et al.*[33] used a toluene solution of boron doped and diethylzinc (DEZ) to obtain a boron-doped transparent conductive zinc oxide (BZO) with a resistivity of 0.0015 Ω cm. Hüpkes J. *et al.*[34] prepared Al-doped ZnO thin coating (AZO), even after 1000 hours of wet and thermal treatment, the coating has a resistivity of 0.0002 Ω cm, and the carrier mobility is still as high as 70 $cm^2\ V^{-1}\ s^{-1}$. Similarly, in this paper, nano-ZnO is added to the coating by chemical conversion, which improves the conductivity of the coating. From the SEM analysis of different treatment times, it can be seen that nano-ZnO is adsorbed on the substrate surface when the coating is formed for 30 s. Due to the small size of nano-ZnO particles, it is easy to adsorb on the surface of the substrate. At the same time, the nano-zno on the surface provides the nucleation center for Na_3AlF_6, so that the microstructure of the coating changes from cobblestone shape to cubic shape. In the previous study,[35] there was a similar situation in which the microstructure of the membrane was changed due to the existence of a new nucleation center. The nano-ZnO primarily occupies the interstices between Na_3AlF_6 crystals, forming an interconnected network of crisscrossing gaps. The presence of nano-ZnO within these gaps effectively establishes a conductive grid, thereby enhancing the coating's conductivity.

According to FTIR and XPS analysis, some chemical reaction occurred between nano-ZnO and trihydroxybenzoic acid, a tannic acid hydrolysis product. This is because the empty orbital of Zn atom in nano-ZnO combined with the lone pair electron on the oxygen atom in the trihydroxybenzoic acid to form an organic complex of Zn. The reaction occurred as follows:

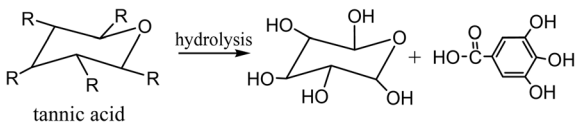

(1)

and

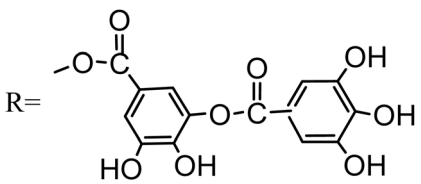

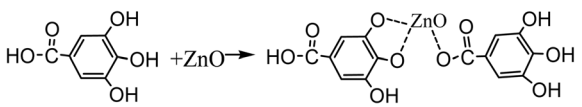

(2)

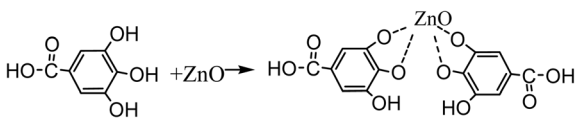

(3)

The sputtering analysis of XPS is a common method to study the coating structure. The Ti/Sn coating was sputtered with argon ions, and the XPS spectra were collected from the same spot on the sample surface.[36] The sputtering rate was 0.51 nm s^{-1} and sputtered 20 times, and the total sputtering depth was

200 nm. As depicted in Fig. 11, the Zn 2p, O 1s, and Na 1s peaks are observed at various etching depths of the coating. The relative atomic concentrations (Table 3) of zinc, oxygen, and sodium were determined from the appropriate core level integrated peak areas. As can be seen from Table 3, for oxygen element, with the increase of sputtering depth, the oxygen content in the coating shows an overall downward trend. This is mainly because the outermost layer of the coating is mainly composed of metal–organic complexes, and with the increase of the coating depth, the content of metal–organic complexes decreases, and the oxygen content decreases. However, when the sputtering depth is greater than 100 nm, the oxygen content remains unchanged at about 7.5%, because after the sputtering depth is greater than the thickness of the metal–organic complex, the coating is dominated by Na_3AlF_6, and the oxygen content tends to be stable. Regarding the zinc content, there is a general upward trend as the sputtering depth increases. When the depth is more than 160 nm, the zinc content fluctuates at about 24%, indicating that there is less zinc in the outermost layer of the coating, and nano-ZnO is mainly distributed in the middle layer. For sodium element, with the increase of sputtering depth, the sodium content shows an overall increasing trend, indicating that the content of Na_3AlF_6 in the coating increases with the increase of depth.

Table 3 Element composition with different sputtering depth

Depth (nm)	10	40	70	100	130	160	190	200
Zn (at/%)	17.53	18.60	22.01	24.71	22.48	24.75	23.99	24.93
Na (at/%)	20.24	26.22	34.41	33.23	33.03	36.15	37.95	37.55
O (at/%)	11.74	8.64	9.10	8.32	7.47	7.77	7.53	7.06

The coating's three-layer structure may be inferred from the aforementioned analysis and SEM of the coating section: the nano ZnO layer close to the substrate, the middle layer of Na_3AlF_6 crystal, and the outermost layer of ZnO and metal organic complex. It can be found that a small amount of nano-ZnO reacts with tannic acid to form complexes on the surface of the coating, and most nano-ZnO is filled between large Na_3AlF_6 particles, forming a conductive path and increasing the electrical conductivity. Nanoparticles (nano-ZnO) have high specific surface energy and are easily adsorbed on the substrate surface, which provides nucleation center for Na_3AlF_6 growth. The coating's growing

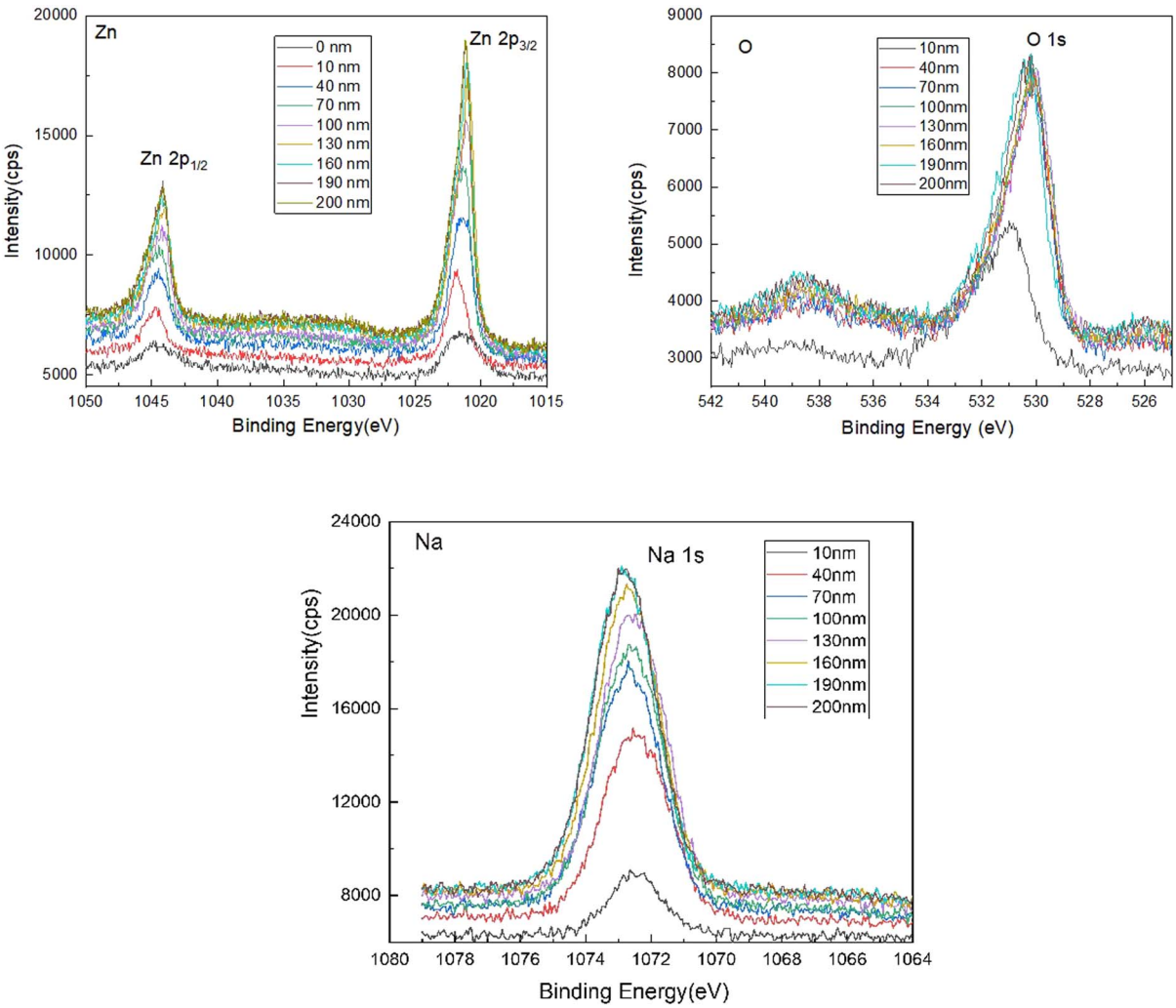

Fig. 11 Zn 2p, O 1s and Na 1s peaks at different etching depths of the coating.

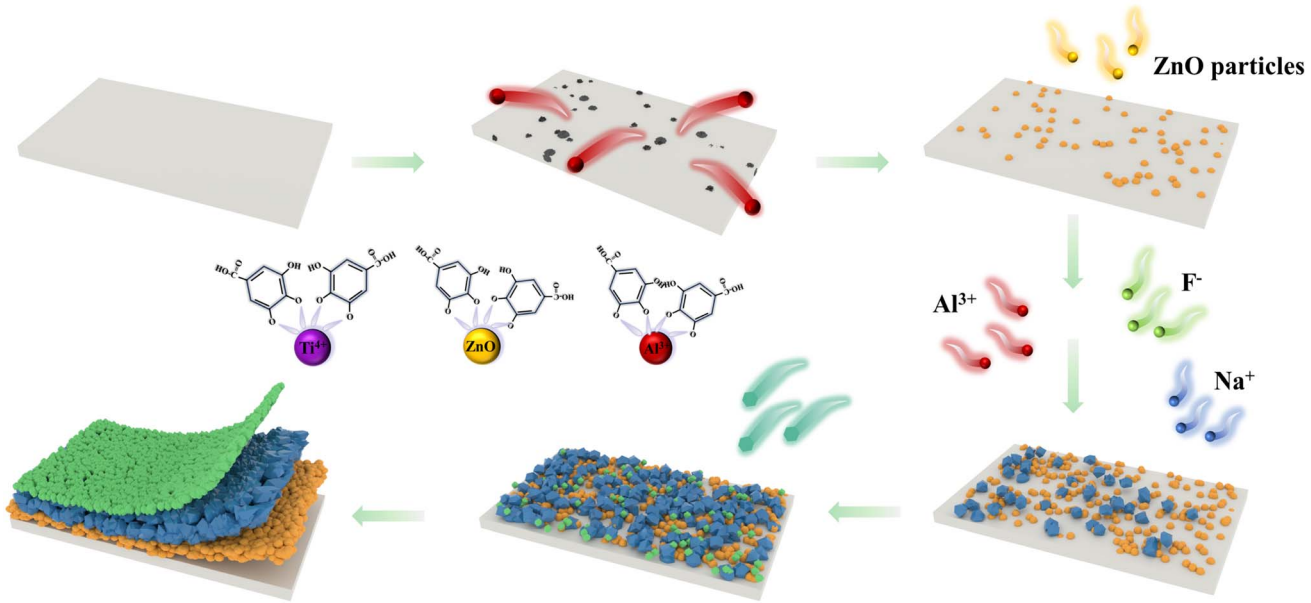

Fig. 12 Coating formation process simulation diagram.

process, depicted in Fig. 12, can be explained as follows. First, the substrate's Al^{3+} dissolves into the solution, and in the meantime, the solution's nano-ZnO starts to deposit on the aluminum substrate's surface. Next, the substrate's surface starts to form the Na_3AlF_6 crystal, which grows steadily until it fills the entire surface. Finally, due to the slow movement of the steric hindrance, the organic complex finally forms and covers the surface of Na_3AlF_6 crystal, and the nano-ZnO in the solution is also deposited on the surface of the coating under the action of the organic complex.

5 Conclusion

(1) By adding nano-ZnO with good conductivity to the solution containing Ti/Zr, a coating with a certain conductivity was prepared on the surface of aluminum alloy. The ECR of the coatings was significantly reduced, and the ECR under 200 psi pressure decreased from 0.1907 Ω in^{-2} without nano-ZnO to 0.00621 Ω in^{-2}. The band gap of the coating decreased from 3.189 eV without nano-ZnO to 2.708 eV with nano-ZnO.

(2) Nano-ZnO has high specific surface energy and is easily adsorbed on the substrate surface, which provides a nucleation center for Na_3AlF_6 growth. A small amount of nano-ZnO reacts with tannic acid to form complexes on the surface of the coating, and most nano-ZnO is filled between large Na_3AlF_6 particles, forming a conductive path and increasing the electrical conductivity.

(3) The coating has a three-layer structure: the nano-ZnO layer close to the substrate, the middle layer of Na_3AlF_6 crystal, and the outermost layer of ZnO and metal–organic complex.

Data availability

The data that support the findings of this study are available from the corresponding author (Min Wang, Winawang@163.com), upon reasonable request.

Conflicts of interest

There are no conflicts to declare.

Acknowledgements

This research has been supported by School research project of Guangzhou City Polytechnic (KYBS2024004), Guangdong Province University Key Field Special (2024ZDZX3095), Tertiary Education Scientific research project of Guangzhou Municipal Education Bureau (2024312013), GuangDong Basic and Applied Basic Research Foundation (2022A1515140043).

References

1 Q. P. Tran, T. S. Chin, Y. C. Kuo, C. X. Jin, T. Trung, C. V. Tuan, *et al.*, Diamond powder incorporated oxide layers formed on 6061 Al alloy by plasma electrolytic oxidation, *J. Alloys Compd.*, 2018, **751**, 289–298.
2 N. Z. Liu, B. Jiang, Z. S. Ji, P. X. Cui, Y. L. Wang and H. Song, Salt spray corrosion and electrochemical corrosion property of anodic oxide films on ADC12 aluminum alloy, *Mod. Phys. Lett. B*, 2022, **36**(04), 2150571.
3 R. V. Lakshmi, S. Sampath and S. T. Aruna, Silica-alumina based sol-gel coating containing cerium oxide nanofibers as a potent alternative to conversion coating for AA2024 alloy, *Surf. Coat. Technol.*, 2021, **411**, 127007.
4 G. Q. Duan, L. X. Yang, S. J. Liao, C. Y. Zhang, X. P. Lu, Y. E. Yang, *et al.*, Designing for the chemical conversion coating with high corrosion resistance and low electrical contact resistance on AZ91D magnesium alloy, *Corros. Sci.*, 2018, **135**, 197–206.
5 J. R. Dong, A. H. Yi, W. F. Li, X. R. Zeng, Z. M. Liao, W. Zhu, *et al.*, Electrical conductivity and corrosion resistance of Mo/

Ti/Mn-based composite conversion films on AZ91D magnesium alloy, *Surf. Coat. Technol.*, 2023, **459**, 129388.

6 M. Kim, L. N. Brewer and G. W. Kubacki, Microstructure and corrosion resistance of chromate conversion coating on cold sprayed aluminum alloy 2024, *Surf. Coat. Technol.*, 2023, **460**, 129423.

7 Z. Q. Gao, D. J. Zhang, Z. Y. Liu, X. G. Li, S. M. Jiang and Q. F. Zhang, Formation mechanisms of environmentally acceptable chemical conversion coatings for zinc: a review, *J. Coat. Technol. Res.*, 2019, **16**, 1–13.

8 E. Chevallier, L. Augée, Q. Boyer, M. P. Labeau and P. Moreau, Fast optimization of polymers to boost adhesion and corrosion prevention in hexafluoride conversion coatings for aluminium, *J. Mater. Sci.*, 2023, **58**, 1368–1381.

9 S. Frangini, L. S. Della and C. Paoletti, Effect of additive particle size on the CuO-accelerated formation of $LaFeO_3$ perovskite conversion coatings in molten carbonate baths, *Surf. Coat. Technol.*, 2019, **374**, 513–520.

10 C. C. Jiang, R. F. Zhu, G. Y. Xiao, Y. Z. Zheng and Y. P. Lu, Effect of Nano-SiO_2 Particles and Sol on Phosphate Conversion Coatings on 35CrMnSi Steel, *J. Electrochem. Soc.*, 2016, **163**, C571–C575.

11 M. M. Bagheri-Mohagheghi, N. Shahtahmasebi, M. R. Alinejad, A. Youssefi and S. M. Shokooh, Fe-doped SnO_2 transparent semi-conducting thin films deposited by spray pyrolysis technique: Thermoelectric and p-type conductivity propertie, *Solid State Sci.*, 2009, **11**(1), 233–239.

12 C. Y. Li, X. L. Fan, L. Y. Cui and R. C. Zeng, Corrosion resistance and electrical conductivity of a nano ATO-doped MAO/methyltrimethoxysilane composite coating on magnesium alloy AZ31, *Corros. Sci.*, 2020, **168**, 108570.

13 Q. S. Jiang, Z. L. Han, Y. F. Yuan, C. Cai, J. Y. Li and Z. Q. Cheng, Controlled preparation and photocatalytic performance of TiO_2/ZnO phase-mixed nanotubes-based nano-spheres, *Mater. Chem. Phys.*, 2022, **279**, 125737.

14 S. Khurshid, H. Latif, S. Rasheed, R. Sharif, A. Sattar and R. J. Amjad, Enhancement in absorption spectrum by ITO coated, down converting glass as a photoanode substrate for efficient PbS/CdS quantum dots sensitized ZnO nano-rods array solar cell, *Opt. Mater.*, 2022, **124**, 111991.

15 C. Y. Tsay and W. Y. Chiu, Coatings. Enhanced Electrical Properties and Stability of P-Type Conduction in ZnO Transparent Semiconductor Thin Films by Co-Doping Ga and N, *Coatings*, 2020, **10**, 1069.

16 R. M. C. Ignacio, C. S. Kim and S. K. Kim, Immunotoxicity of metal oxide nanoparticle: zinc oxide, *Mol. Cell. Toxicol.*, 2014, **10**, 237–244.

17 R. L. Yan, T. Takahashi, H. Zeng, T. Hosomi, M. Kanai, G. Z. Zhang, *et al.*, Robust and Electrically Conductive ZnO Thin Films and Nanostructures: Their Applications in Thermally and Chemically Harsh Environments, *ACS Appl. Electron. Mater.*, 2021, **3**(7), 2925–2940.

18 S. H. Jeong, J. W. Lee, S. B. Lee and J. H. Boo, Deposition of aluminum-doped zincoxide films by RF magnetron sputtering and study of their structural, electrical and optical properties, *Thin Solid Films*, 2003, **435**, 78–82.

19 A. H. Yi, W. F. Li, J. Du and S. L. Mu, Preparation and properties of chrome-free colored Ti/Zr based conversion coating on aluminum alloy, *Appl. Surf. Sci.*, 2012, **258**, 5960–5964.

20 S. J. Mao, W. F. Li, X. R. Zeng, A. H. Yi, Z. M. Liao and W. Zhu, Multiple transitional metal oxides conversion coating on AA6063 toward corrosion protection and electrical conductivity, *Surf. Coat. Technol.*, 2020, **397**, 125819.

21 X. M. Chen, G. Y. Li, J. S. Lian and Q. Jiang, Study of the formation and growth of tannic acid based conversion coating on AZ91D magnesium alloy, *Surf. Coat. Technol.*, 2009, **204**(5), 736–747.

22 X. M. Chen, G. Y. Li, J. S. Lian and Q. Jiang, An organic chromium-free conversion coating on AZ91D magnesium alloy, *Appl. Surf. Sci.*, 2008, **255**(5), 2322–2328.

23 Z. Y. Han, J. C. Zhang, X. Y. Yang, H. Zhu and W. L. Cao, Synthesis and photoelectric property of poly (3-octylthiophene)/zinc oxide complexes, Solar Energy Materials and Solar Cells, *Sol. Energy Mater. Sol. Cells*, 2010, **94**, 194–200.

24 L. Margielewski, R. Stanecka-Badura, S. Plaza and W. Kozlowski, Preparation and tribological properties of zinc dialkyl(aryl)ethoxy dithiophosphates, *Ind. Lubr. Tribol.*, 2012, **64**(4), 187–195.

25 M. Li, B. Peng, L. Y. Chai, N. Peng, X. D. Xie and H. Yan, Technological mineralogy and environmental activity of zinc leaching residue from zinc hydrometallurgical process, *Trans. Nonferrous Met. Soc.*, 2013, **23**(5), 1480–1488.

26 J. J. M. Ferreira, M. Oliveira, G. F. Trindade and L. C. Santos, Development and characterisation of zinc oxalate conversion coatings on zinc, *Corros. Sci.*, 2018, **137**, 13–32.

27 J. Duchoslav, R. Steinberger, M. Arndt and D. Stifter, XPS study of zinc hydroxide as a potential corrosion product of zinc: Rapid X-ray induced conversion into zinc oxide, *Corros. Sci.*, 2014, **82**, 356–361.

28 S. Giancaterina, E. M. Bachari, G. Baud, M. Jacquet, C. Perrin and A. S. Ben, Elaboration and adhesion of zinc oxide coatings on poly-ether-ether-ketone films, *Surf. Coat. Technol.*, 2001, **138**(1), 84–94.

29 H. F. Haneef, A. M. Zeide and O. D. Jurchescu, Charge carrier traps in organic semiconductors: a review on the underlying physics and impact on electronic devices, *J. Mater. Chem. C*, 2020, **8**(3), 759–787.

30 A. Dolgonos, T. O. Mason and K. R. Poeppelmeier, Direct optical band gap measurement in polycrystalline semiconductors: A critical look at the Tauc method, *J. Solid State Chem.*, 2016, **240**, 43–48.

31 P. R. Jubu, F. K. Yam, V. M. Igba and K. P. Beh, Tauc-plot scale and extrapolation effect on bandgap estimation from UV-vis-NIR data - A case study of beta-Ga_2O_3, *J. Solid State Chem.*, 2020, **290**, 121576.

32 S. Pawaria, J. Ahlawat, M. Bala, S. Dahiy, A. Ohlan, R. Punia, *et al.*, Structural and optical characterization of semiconducting lithium modified zinc borate glassy system for UV band reject filter, *J. Mol. Struct.*, 2022, **1270**, 133836.

33 T. Shirahata, T. Kawaharamura, S. Fujita and H. Orita, Transparent conductive zinc-oxide-based films grown at low temperature by mist chemical vapor deposition, *Thin Solid Films*, 2015, **59**, 30–38.
34 J. Hüpkes, J. I. Owen, M. Wimmer, F. Ruske, D. Greiner, R. Klenk, *et al.*, Damp heat stable doped zinc oxide films, *Thin Solid Films*, 2014, **555**, 48–52.
35 A. H. Yi, W. F. Li, J. Du and S. L. Mu, Effects of Mn^{2+} on the chrome-free colored Ti/Zr-based conversion coating on 6063 aluminum alloy, *Surf. Interface Anal.*, 2015, **47**(9), 863–870.
36 J. Moo, Z. Awaludin, T. Okajima and T. Ohsaka, An XPS depth-profile study on electrochemically deposited TaO (x), *J. Solid State Electrochem.*, 2013, **17**, 3115–3123.